

Nonuniform Electro-osmotic Flow Drives Fluid-Structure Instability

Evgeniy Boyko,^{1,‡} Ran Eshel,^{1,‡} Amir D. Gat,^{1,*} and Moran Bercovici^{1,2,†}

¹*Faculty of Mechanical Engineering, Technion—Israel Institute of Technology, Haifa 3200003, Israel*

²*Department of Mechanical Engineering, The University of Texas at Austin, Austin, Texas 78712, USA*

 (Received 22 June 2019; published 14 January 2020)

We demonstrate the existence of a fluid-structure instability arising from the interaction of electro-osmotic flow with an elastic substrate. Considering the case of flow within a soft fluidic chamber, we show that above a certain electric field threshold, negative gauge pressure induced by electro-osmotic flow causes the collapse of its elastic walls. We combine experiments and theoretical analysis to elucidate the underlying mechanism for instability and identify several distinct dynamic regimes. The understanding of this instability is important for the design of electrokinetic systems containing soft elements.

DOI: 10.1103/PhysRevLett.124.024501

Introduction.—Electro-osmotic flow (EOF) arises over electrically charged surfaces due to interaction of an externally applied electric field with the net charge in the electric double layer on a surface. Since its discovery by Reuss in 1809 [1], EOF has become a common method to manipulate fluids in microfluidic and lab-on-a-chip devices [2]. In many microfluidic applications, EOF acts against hydraulic resistance, resulting in an internal pressure distribution, which can be (gauge) positive or negative depending on the direction of the flow and the associated boundary conditions [2]. Since electro-osmotic flow rate scales as $\tilde{h}\tilde{u}_{\text{EOF}}$, and pressure driven flow rate scales as $\tilde{p}\tilde{h}^3/\tilde{\mu}\tilde{l}$, conservation of mass dictates a characteristic pressure of [3]

$$\tilde{p} \sim \frac{\tilde{\mu}\tilde{l}}{\tilde{h}^2}\tilde{u}_{\text{EOF}}, \quad (1)$$

where \tilde{u}_{EOF} is the electro-osmotic slip velocity, \tilde{h} is the height of the channel, \tilde{l} is the characteristic streamwise length scale, and $\tilde{\mu}$ is the fluid viscosity.

Many microfluidic configurations are fabricated from soft materials such as poly(dimethylsiloxane) (PDMS) [4], and thus may deform due to fluid flow within the device. Such deformations were also recently studied in the context of EOF-driven flows by Mukherjee *et al.* [5], de Rutte *et al.* [6], and Boyko *et al.* [7]. In all those studies, the fluid-structure interaction exhibited stable behavior.

In this Letter, we show for the first time that such electro-osmotic flow systems exhibit fluid-structure instability. Negative pressures induced by EOF lead to deformation of the elastic walls, decreasing the fluidic film thickness, \tilde{h} . In accordance with Eq. (1), this results in the pressure becoming increasingly negative, acting to further reduce the gap. Using experimental observations and theoretical predictions, we show the existence of an instability wherein

small changes in the electric field lead to large changes in the deformation and ultimately the collapse of the elastic wall. We provide insight into the physical mechanisms underlying it and demonstrate that above a certain electric field threshold, the system switches from a stable behavior to an unstable one, characterized by a metastable bottleneck period. When the electric field is further increased, the bottleneck disappears and the system transitions to exhibit an immediate collapse of the elastic wall.

Experimental.—To observe the dynamics of an elastic boundary subjected to negative pressure induced by non-uniform EOF, we designed an experimental system, shown in Fig. 1. The system consists of a $\tilde{h}_i = 171 \mu\text{m}$ deep fluidic chamber with a thin, $40 \mu\text{m}$, elastic ceiling made of polydimethylsiloxane (PDMS). At the far edges of the 30 mm long chamber, there are two reservoirs through which the driving electric field is applied to the system. The bottom of the fluidic chamber is a glass slide, half of which is coated with poly(allylamine hydrochloride) (PAH) [8], a positively charged polyelectrolyte, changing the glass's native negative surface charge to a positive one. The elastic ceiling is supported everywhere by a rigid acrylic frame, except for a $15 \times 15 \text{ mm}$ region whose center is aligned with the surface charge discontinuity on the glass. On top of this region, we placed a 0.2 g, $10 \times 10 \text{ mm}$ rigid acrylic plate, which stretches the elastic ceiling and reduces the liquid thickness to $\tilde{h}_0 = 94 \mu\text{m}$ at rest. We measure the vertical translation of the acrylic plate in time, $\tilde{h}(\tilde{t})$, by monitoring the change in the point spread function (PSF) of fluorescent microbeads deposited on its top surface, as shown Fig 1(b). To enable measurement over the entire range of motion of the plate, we modify the PSF using a cylindrical lens, placed in front of the camera sensor [9]. At each time point, the image of each bead's PSF is compared against a pre-established calibration curve yielding its vertical position. We fill the fluidic chamber with

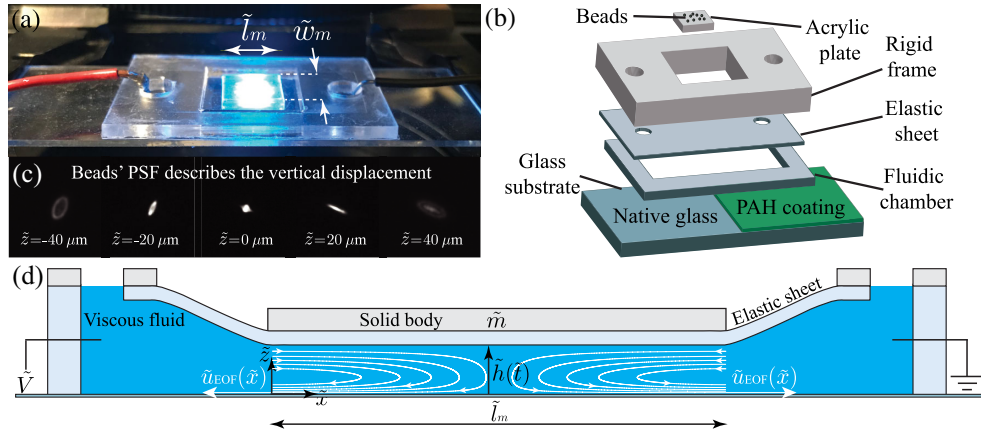


FIG. 1. Illustration of the configuration used for experiments and modeling. (a) Image of the experimental device, (b) exploded isometric view showing its different layers, and (d) two-dimensional model and key parameters used for the theoretical analysis. The device consists of a microfluidic chamber chemically functionalized to produce nonuniform EOF. The chamber’s floor is fixed while its ceiling can move vertically, supported by an elastic sheet. Upon application of an electric field, flow is driven from the center to the edges of the chamber, resulting in negative pressure and downward motion of the ceiling. (c) We monitor the height of the ceiling $\tilde{h}(\tilde{t})$ in time by capturing the change in the point spread function (PSF) of beads deposited on top of it, and observe its collapse onto the bottom surface when instability is triggered.

10 mM histidine, providing simultaneously low conductivity and high buffering capacity, and apply a set of fixed voltages between the two reservoirs. The direction of the electric field is set such that the established EOF velocity is directed from the center of the chamber outward, thus inducing a negative pressure within the chamber.

Experimental observations.—Figure 2(a) presents one dataset of experimental measurements, showing the height of the plate relative to the bottom glass surface as a function of time for several applied voltages. Additional datasets exhibiting identical behavior are provided in the Supplemental Material [10]. We observe three distinct regimes for the dynamics of the plate. (i) Below a certain electric field threshold value (here approximately $\tilde{E}_{CR} = -2.23 \times 10^4 \text{ V m}^{-1}$), the plate is pulled downward and achieves a new steady-state position where the hydrodynamic forces are balanced by the restoring force of the elastic membrane. (ii) For electric fields above this threshold, the plate appears to be reaching a steady state as it lingers at a nearly fixed height for a significant duration of time, but finally, without any external interference to the system, it accelerates down and rapidly collapses onto the bottom surface. (iii) As the electric field is increased this metastable “bottleneck time,” in which the plate descent is slowed down, shortens. For sufficiently high electric fields it completely disappears and the plate collapses to the floor immediately after application of the electric field. Figure 3(a) presents the height of the plate at the end of the experiment (after 195 s) as a function of the applied electric field, distinctly indicating the onset of instability. While for an electric field of $\tilde{E}_{CR} = -2.23 \times 10^4 \text{ V m}^{-1}$ the system reaches a steady state at a moderate deformation, an increase of only 1.3% in the magnitude of the field results

in an abrupt change in behavior, collapsing the plate onto the bottom surface. This can also be observed in the grayed-out region of Fig. 2(a), where we allowed a longer measurement time in order to capture as accurately as possible the onset of instability.

Theoretical model.—To provide further insight into the physical behavior of the system, we formulate a one-dimensional model describing the temporal evolution of the film thickness $\tilde{h}(\tilde{t})$. We consider a viscous liquid film confined between a rigid surface and a rigid body of mass \tilde{m} and length \tilde{l}_m , placed on the top of an elastic sheet, which we model as a linear spring with stiffness \tilde{k} , as shown in Fig. 1(d). The liquid film is connected to two fluidic reservoirs at a distance \tilde{L} from one another, through which the electric field is applied. We employ a Cartesian coordinate system (\tilde{x}, \tilde{z}) , as indicated in Fig. 1(d). As in our experimental setup, we prescribe a nonuniform electroosmotic slip velocity $\tilde{u}_{EOF}(\tilde{x})$ on the bottom rigid surface, which in the thin double-layer limit, can be described by the Helmholtz-Smoluchowski equation [14],

$$\tilde{u}_{EOF} = -\frac{\tilde{\epsilon}\tilde{\zeta}\tilde{E}}{\tilde{\mu}}, \quad (2)$$

where $\tilde{\epsilon}$ is the liquid permittivity, $\tilde{\zeta}(\tilde{x})$ is the zeta potential distribution on the surface, and \tilde{E} is the imposed electric field. While the experimental system is three dimensional, we still expect to capture the key properties of the system from a two-dimensional analysis in the $\tilde{x} - \tilde{z}$ plane, since the EOF-induced pressure gradients are primarily along the \tilde{x} axis.

Applying the lubrication approximation to the flow field, we relate the fluidic pressure \tilde{p} to the gap height $\tilde{h}(\tilde{t})$ [10],

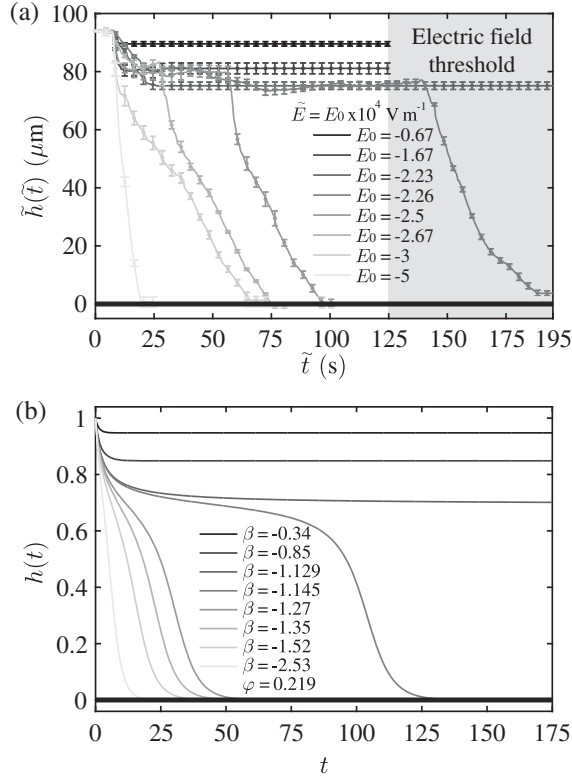


FIG. 2. Time evolution of the fluidic gap resulting from nonuniform electro-osmotic flow. (a) The experimentally observed temporal evolution of the film thickness $\tilde{h}(\tilde{t})$ for various values of \tilde{E} and (b) the corresponding theoretically predicted evolution of $h(t)$ for various values of β , indicating three distinct dynamic behaviors. Below the threshold values of $\tilde{E}_{\text{CR}} = -2.23 \times 10^4 \text{ V m}^{-1}$ or $\beta_{\text{CR}} = -1.129$, the ceiling approaches a stable steady-state height. Setting \tilde{E} or β to slightly above their threshold values ($\tilde{E} = -2.26 \times 10^4 \text{ V m}^{-1}$ and $\beta = -1.145$) triggers instability characterized by a bottleneck period. For higher values of \tilde{E} or β (e.g., for $\tilde{E} = -5 \times 10^4 \text{ V m}^{-1}$ or $\beta = -2.53$) the bottleneck phase disappears and the ceiling immediately collapses onto the rigid floor. Error bars in (a) indicate a 95% confidence of the mean position of nine beads measured at each time point. The grayed-out region highlights two experiments in which the driving field differs by only 1.3%, capturing the threshold of instability and leading to a longer bottleneck due to the proximity to this value.

$$\frac{d\tilde{h}(\tilde{t})}{d\tilde{t}} - \frac{\tilde{h}(\tilde{t})^3}{12\tilde{\mu}} \frac{\partial^2 \tilde{p}(\tilde{x}, \tilde{z}, \tilde{t})}{\partial \tilde{x}^2} + \frac{1}{2} \tilde{h}(\tilde{t}) \frac{d\tilde{u}_{\text{EOF}}(\tilde{x})}{d\tilde{x}} = 0. \quad (3)$$

Solving Eq. (3) for the pressure \tilde{p} at $\tilde{z} = \tilde{h}$, and then integrating the result with respect to \tilde{x} from 0 to \tilde{l}_m while using the global mass conservation, provides the force \tilde{F}_p that the fluidic pressure exerts on the rigid body (see Ref. [10]),

$$\tilde{F}_p(\tilde{t}) = -\frac{\tilde{\mu}\tilde{l}_m^3}{\tilde{h}(\tilde{t})^3} \frac{d\tilde{h}(\tilde{t})}{d\tilde{t}} + \frac{6\tilde{\mu}\tilde{B}}{\tilde{h}(\tilde{t})^2} + \chi\tilde{\rho}\tilde{g}\tilde{l}_m[\tilde{h}_i - \tilde{h}(\tilde{t})], \quad (4)$$

where $\chi = 1 + [\tilde{l}_m/(\tilde{L} - \tilde{l}_m)]$ and \tilde{B} is defined as

$$\tilde{B} = -\frac{\tilde{\epsilon}\tilde{E}}{\tilde{\mu}} \left(\int_0^{\tilde{l}_m} \left(\int_0^{\tilde{x}} \tilde{\zeta}(\tilde{\xi}) d\tilde{\xi} \right) d\tilde{x} - \frac{\tilde{l}_m}{2} \int_0^{\tilde{l}_m} \tilde{\zeta}(\tilde{\xi}) d\tilde{\xi} \right). \quad (5)$$

The first term on the right-hand side of Eq. (4) represents the viscous resistance, the second term represents the electro-osmotic force which can be either attractive or repulsive depending on the sign of \tilde{B} , and the last term represents the restoring effect of the hydrostatic pressure.

In addition to the pressure induced by the nonuniform electro-osmotic flow, a dielectric force arising from the Maxwell stresses also acts on the plate. Since the permittivity of the PDMS and air are negligible compared to that of the water, we may neglect their contributions to the Maxwell stress and express the (upward directed) dielectric force \tilde{F}_d as [15]

$$\tilde{F}_d = \frac{1}{2} \tilde{\epsilon}\tilde{E}^2\tilde{l}_m. \quad (6)$$

Neglecting the plate's inertia, the force balance on the rigid plate, accounting for the fluidic, dielectric, and the elastic forces, yields a governing equation for the gap $\tilde{h}(\tilde{t})$ [10]

$$-\frac{\tilde{\mu}\tilde{l}_m^3}{\tilde{h}(\tilde{t})^3} \frac{d\tilde{h}(\tilde{t})}{d\tilde{t}} + \frac{6\tilde{\mu}\tilde{B}}{\tilde{h}(\tilde{t})^2} + \frac{1}{2} \tilde{\epsilon}\tilde{E}^2\tilde{l}_m + \tilde{k}_g[\tilde{h}_0 - \tilde{h}(\tilde{t})] = 0, \quad (7)$$

where $\tilde{k}_g = \tilde{k} + \chi\tilde{\rho}\tilde{g}\tilde{l}_m$ is the generalized spring stiffness consisting of contributions of elasticity and gravity, and $\tilde{h}_0 = \tilde{h}_i - (\tilde{m}\tilde{g}/\tilde{k}_g)$ is the liquid film thickness when the plate is at rest.

Equation (7) resembles nonlinear evolution equations encountered in a range of instability problems such as electrostatic MEMS actuators [16], and elastocapillarity coalescence [17]. Here the different terms in Eq. (7) represent the coupling between viscous resistance, the electro-osmotic and dielectric forces, and the restoring effects of the elasticity and gravity. As we show in the Supplemental Material [10], the case of constant current results in yet another variant of the equation, with different scaling for the actuation force (\tilde{h}^{-3}).

We introduce the nondimensional variables $x = \tilde{x}/\tilde{l}_m$, $h = \tilde{h}/\tilde{h}_0$, and $t = \tilde{t}/\tilde{t}^*$, where $\tilde{t}^* = \tilde{\mu}\tilde{l}_m^3/\tilde{k}_g\tilde{h}_0^3$ is the viscous-elastic timescale obtained by balancing the first and the fourth terms in Eq. (7). With this nondimensionalization, the governing Eq. (7) reads

$$\frac{1}{h^3} \frac{dh}{dt} = \frac{4}{27} \frac{\beta}{h^2} + \frac{4}{27} \varphi \beta^2 + 1 - h, \quad (8)$$

subject to the initial condition $h(t=0) = 1$. Here $\beta = 81\tilde{B}/(2\tilde{k}_g\tilde{h}_0^3/\tilde{\mu})$ represents the ratio of electro-osmotic to

elastic forces, and $\varphi = \tilde{k}_g \tilde{h}_0^5 / (486 \lambda^2 \tilde{\epsilon} \tilde{\zeta}^2 \tilde{l}_m^3)$ is a strictly positive parameter, wherein $\lambda = \tilde{B} / (\tilde{\epsilon} \tilde{\zeta} \tilde{E} \tilde{l}_m^2 / \tilde{\mu})$. We note that while β changes by manipulation of the applied electric field, the parameters φ and λ remain constant for a given configuration.

To understand the physical mechanisms underlying the instability, we perform a linear stability analysis of Eq. (8). We consider a small perturbation of the rigid body from its equilibrium height h_{ss} , by setting $h(t) = h_{ss}(1 + \epsilon_0 e^{\sigma t})$, where $\epsilon_0 \ll 1$ is some small perturbation and σ is the nondimensional growth rate. We obtain that the growth rate σ is [10]

$$\sigma = -\frac{8}{27}\beta - h_{ss}^3, \quad (9)$$

indicating that positive values of β , corresponding to positive (upward) deformation always result in a stable system, whereas negative values of β may destabilize it. Equating σ [Eq. (9)] to zero, and using the implicit equilibrium solution for h_{ss} as a function of β and φ , $(4/27)\beta/h_{ss}^2 + (4/27)\varphi\beta^2 + 1 - h_{ss} = 0$, we find that the critical steady-state height h_{ssCR} and the corresponding threshold value β_{CR} , are determined from the equations $\beta_{CR} = -[1 + (4/27)\varphi\beta_{CR}^2]^3$ and $h_{ssCR} = 2/3[1 + (4/27)\varphi\beta_{CR}^2]$. Using physical and geometrical parameters from our experimental setup [10], we estimate $\varphi = 0.219$ and obtain that $h_{ssCR} = 0.694$ and $\beta_{CR} = -1.129$. Using the experimentally measured values for $\tilde{\zeta}$, \tilde{h}_0 , \tilde{k}_g , and $\tilde{\mu}$, the latter corresponds to an electric field of $\tilde{E}_{CR, \text{Theory}} = -52927$ V/m, which is on the same order of magnitude as the experimentally observed $\tilde{E}_{CR, \text{Exp}} = -22300$ V/m. Despite the theoretical analysis being purely one dimensional in space, it provides a reasonable prediction for the threshold electric field.

Figure 3(b) presents the steady-state height h_{ss} as a function of β , for $\varphi = 0.219$. The dashed red line represents the steady-state solutions of Eq. (8). For $\beta > \beta_{CR} = -1.129$, there are two real steady-state solutions, one of which is linearly stable and the other is linearly unstable. At $\beta_{CR} = -1.129$, these two solutions coincide and disappear at a saddle-node (fold) bifurcation with $h_{ssCR} = 0.694$. Black dots represent the results of a numerical simulation showing the collapse dynamics, consistent with the results of linear stability analysis.

To explain the experimentally observed temporal evolution of the film thickness showing strong dependence on the applied electric field [see Fig. 2(a)], we solve numerically the nonlinear evolution equation (8) for fixed values of β . It is convenient to discuss a normalized electric field difference δ defined as

$$\delta = \frac{\tilde{E} - \tilde{E}_{CR}}{\tilde{E}_{CR}} = \frac{\beta - \beta_{CR}}{\beta_{CR}}, \quad (10)$$

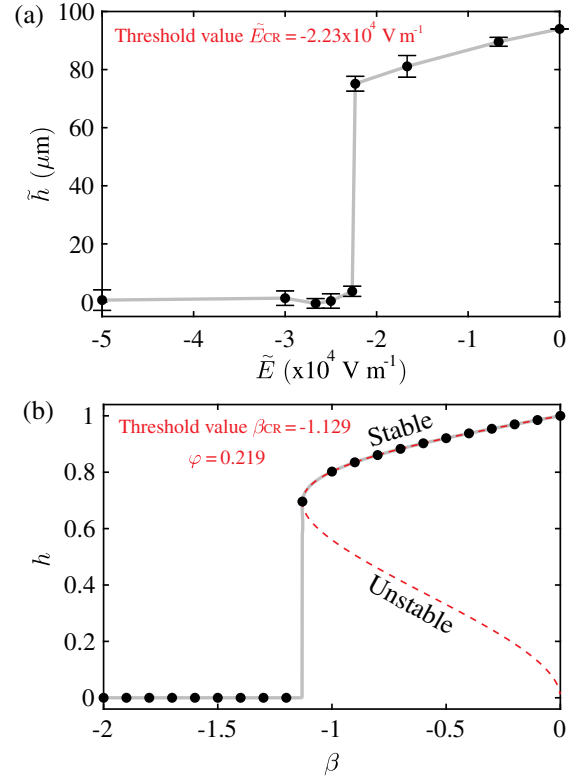


FIG. 3. Theoretical and experimental observation of a threshold electric field for instability. (a) The experimentally observed height \tilde{h} at the end of each experiment, as a function of applied electric field \tilde{E} . Error bars indicate a 95% confidence on the mean based on four experiments [10]. (b) The theoretically predicted steady-state height h as a function of β . The red dashed line represents the results of a linear stability analysis, whereas black dots represent the results of the dynamic simulation. At $\beta_{CR} = -1.129$ the stable equilibrium intersects an unstable solution and disappears at a saddle-node bifurcation [10]. Above the threshold values of $\tilde{E}_{CR} = -2.23 \times 10^4$ V m $^{-1}$ and $\beta_{CR} = -1.129$, no equilibrium solutions exist and the system exhibits instability that collapses the ceiling onto the floor. Gray lines in both subfigures were added to guide the eye.

so that $\beta = \beta_{CR}(1 + \delta)$ and $\tilde{E} = \tilde{E}_{CR}(1 + \delta)$, and the instability occurs for $\delta > 0$.

Figure 2(b) presents the time evolution of the gap $h(t)$ for different values of β , with $\varphi = 0.219$. Our theoretical analysis identifies the three distinct dynamic behaviors observed in the experiments, with β_{CR} ($\delta = 0$) serving as the threshold parameter. The analysis shows that a bottleneck behavior is obtained only for very small values of β above this threshold, i.e., $0 < \delta \ll 1$. Furthermore, our analysis explains the significant slow down of the plate as it approaches the surface: the viscous resistance increases as h^{-3} , while the electro-osmotic attraction increases as h^{-2} , leading to an exponential decay. Figure 2 also indicates a strong dependence of the total collapse duration on δ . In the Supplemental Material [10] we seek to quantify

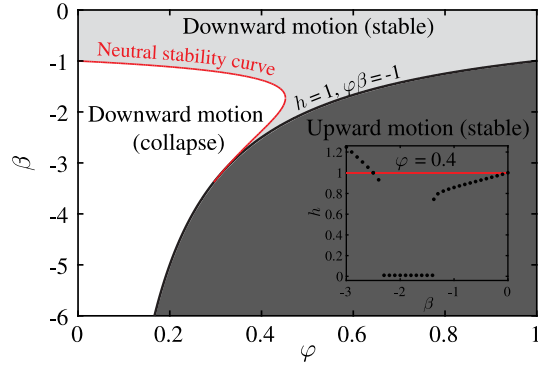


FIG. 4. Stability map showing three distinct regions as a function of β and φ . The light gray region corresponds to a stable downward motion due to negative EOF-induced pressure, the dark gray region corresponds to a stable upward motion where the dielectric force overcomes the EOF-induced negative pressure, and the white region corresponds to an unstable collapse of the plate toward the floor. The inset presents the steady-state height of the plate as a function of β for $\varphi = 0.4$, showing the transition between regimes as β is made more negative.

this total collapse time, which we express as a combination of the bottleneck time and the exponential decay time. Figure S7(a) [10] compares the experimental and theoretically predicted collapse duration, with good agreement over 2 orders of magnitude in δ .

Expanding our theoretical analysis to values of β and φ beyond those of our experimental setup, we present in Fig. 4 a stability diagram for different values of β and φ , showing three distinct regions. For sufficiently small $|\beta|$ values, the dielectric forces are negligible and the system reaches a negative stable deformation (light gray region), characterized by a balance between the electro-osmotic pulldown and the elastic restoring force. For small values of φ and sufficiently negative values of β (white region), the EOF-driven instability emerges and triggers the collapse of the plate. While our experiments could be mapped to these two regions, Fig. 4 reveals an additional region which our setup cannot cover. For large values of φ and sufficiently negative values of β (dark gray region), the upward directed dielectric force overcomes the EOF-induced negative pressure, resulting in a positive stable deformation. The interfaces between the regions are defined by two curves: $\beta = -[1 + (4/27)\varphi\beta^2]^3$ (red curve) indicates the transition from a stable to the unstable downward motion of the plate and is obtained from linear stability analysis. $\varphi\beta = -1$ (black curve) indicates the transition from a downward to the upward motion, obtained by requiring $h = 1$ in Eq. (8) [10]. As Fig. 4 (inset) indicates, decreasing the value of β at a given φ results in the system passing through multiple regions. We stress that, for any value of φ , there exists a sufficiently large electric field for which the dielectric force will always dominate over the electro-osmotic force, leading to the upward movement of the plate.

Summary and conclusions.—EOF systems are typically considered to be symmetric; i.e., inversion of the electric field also inverts the direction of the flow. The coupling with elasticity breaks this symmetry, as is the case in other problems involving flow and elasticity, such as microswimmers or flows in the alveoli. This asymmetry is greatly enhanced by the instability we presented here, and the system can be considered as a deformation-based diode; for an electric field acting in a direction creating positive pressure, flow will be allowed through the channel. However, for an electric field acting in the opposite direction, the instability will be triggered, and the collapse of the channel walls will stop the flow. Interestingly, due to the competition between EOF-induced pressure and dielectrophoretic forces, our theory predicts that the direction of deformation can also be inverted not only by inverting the direction of the field, but also by modifying its magnitude, where for a sufficiently large field the instability is avoided and a positive deformation is obtained. Within the possible experimental parameters of our experiment, we could not however obtain sufficiently high electric fields to observe this, but also note that at such fields additional phenomena such as Joule heating may affect the dynamics, and those were not taken into account in our analysis.

One could consider expansion of this study to multiple chambers, in parallel or in series, which interact with one another through both the fluid flow and the electric current distribution. Such a configuration would exhibit spatio-temporal propagation of the flow and electric fields, and of the resulting instability. One limit of such a distributed system would be an elastic substrate that can deform arbitrarily, where the interplay between EOF-induced pressures and elastic deformation may lead to additional rich physics such as moving contact points involving triple phase contact lines.

This project has received funding from the European Research Council (ERC) under the European Union’s Horizon 2020 Research and Innovation Programme, Grant Agreement No. 678734 (MetamorphChip). E. B. is supported by the Adams Fellowship Program of the Israel Academy of Sciences and Humanities.

*Corresponding author.
amirgat@technion.ac.il

†Corresponding author.
mberco@technion.ac.il

‡These authors contributed equally to this work.

- [1] F.F. Reuss, Mem. Soc. Imp. Nat. Moscou **2**, 327 (1809).
- [2] H. A. Stone, A. D. Stroock, and A. Ajdari, *Annu. Rev. Fluid Mech.* **36**, 381 (2004).
- [3] D. J. Laser and J. G. Santiago, *J. Micromech. Microeng.* **14**, R35 (2004).

-
- [4] G. M. Whitesides, *Nature (London)* **442**, 368 (2006).
- [5] U. Mukherjee, J. Chakraborty, and S. Chakraborty, *Soft Matter* **9**, 1562 (2013).
- [6] J. M. de Rutte, K. G. Janssen, N. R. Tas, J. C. Eijkel, and S. Pennathur, *Microfluid. Nanofluid.* **20**, 150 (2016).
- [7] E. Boyko, R. Eshel, K. Gommed, A. D. Gat, and M. Bercovici, *J. Fluid Mech.* **862**, 732 (2019).
- [8] F. Paratore, E. Boyko, G. V. Kaigala, and M. Bercovici, *Phys. Rev. Lett.* **122**, 224502 (2019).
- [9] R. Barnkob, C. J. Kähler, and M. Rossi, *Lab Chip* **15**, 3556 (2015).
- [10] See Supplemental Material at <http://link.aps.org/supplemental/10.1103/PhysRevLett.124.024501> for further details of experiments and theoretical calculations, which includes Refs. [11–13].
- [11] L. G. Leal, *Advanced Transport Phenomena* (Cambridge University Press, Cambridge, England, 2007).
- [12] S. H. Strogatz, *Nonlinear Dynamics and Chaos: With Applications to Physics, Biology, Chemistry, and Engineering* (Addison-Wesley, Reading, MA, 1994).
- [13] M. Gomez, D. E. Moulton, and D. Vella, *J. Micromech. Microeng.* **28**, 015006 (2018).
- [14] R. J. Hunter, *Foundations of Colloid Science* (Oxford University Press, New York, 2001).
- [15] L. D. Landau and E. M. Lifshitz, *Electrodynamics of Continuous Media* (Pergamon Press, Bristol, 1960).
- [16] G. M. Rebeiz, *RF MEMS: Theory, Design, and Technology* (John Wiley & Sons, Hoboken, 2004).
- [17] K. Singh, J. R. Lister, and D. Vella, *J. Fluid Mech.* **745**, 621 (2014).